

Absorbing phase transition with a continuously varying exponent in quantum contact process

Minjae Jo,¹ K. Choi,¹ and B. Kahng^{1,*}

¹CCSS, CTP and Department of Physics and Astronomy, Seoul National University, Seoul 08826, Korea

Phase transitions in dissipative quantum systems are intriguing because they are induced by competition between coherent quantum and incoherent classical fluctuations. Here, we investigate the interplay of the quantum and classical absorbing phase transitions arising in the quantum contact process (QCP) in one dimension. The Lindblad equation contains two model parameters, ω and κ , which adjust the contributions of the quantum and classical effects, respectively. We find a characteristic value κ_* that separates a novel class of QCP from the directed percolation (DP) class. In the region $[0, \kappa_*]$, the exponent α associated with the density of active sites varies continuously, whereas for $\kappa > \kappa_*$, α has the DP value. We use the neural network machine learning technique to identify the transition point $\omega_c(\kappa)$ and determine the correlation length exponent. By performing extensive quantum jump Monte Carlo simulations at $\omega_c(\kappa)$, we successfully determine all the other critical exponents of the QCP in one dimension. Finally, we remark that the behavior of the continuously varying exponent is similar to that in the tricritical contact process with long-range interactions.

Introduction – Quantum critical phenomena in nonequilibrium systems have attracted considerable attention recently in the physics community [1–19] with the development of experimental techniques in cold atomic physics such as trapped ions [14] and lattices of ultracold ions [15–17]; driven circuit quantum electrodynamics systems [18]; and semiconductor microcavities [19]. The quantum criticality in the equilibrium state may be perturbed by the external environment, and thus the combined system is left in a non-equilibrium state. An associated phenomenon is the quantum phase transition in a Josephson junction from a normal to a superconducting state depending on the value of an external shunt resistor [20]. Here, we are interested in dissipative phase transitions arising from competition between the coherent Hamiltonian dynamics and incoherent dissipation process [20–32]. For these systems, questions arise as to whether the competition between quantum and classical fluctuations produces novel universal behavior [25, 26] and the conditions under which they exhibit classical critical behavior in terms of the loss rates to the environment [20, 30, 31, 33].

Here, we aim to answer these questions by considering the quantum contact process [34–40] in one dimension (1D-QCP). The contact process (CP) is a prototypical model exhibiting a nonequilibrium phase transition. Each element of the system is in an active or inactive state, and its state changes according to the CP model [41–47]. When all the elements are in the inactive state, the system becomes trapped in a frozen configuration. Examples include the catalytic reactions occurring during the oxidation of carbon monoxide on a platinum surface [42]. This CP dynamics was realized recently using the spin orientations of Rydberg atoms in one dimension [48]. Thus, the classical CP problem extends to the CP in dissipative quantum systems in one dimension, that is, the 1D-QCP. The dynamics of the 1D-QCP model is described by the Lindblad equation, which consists of a coherent Hamiltonian and incoherent dissipative terms. Their contributions to the overall dynamics are adjusted by the model parameters ω (for the coherent quantum effect) and κ (for the incoherent classical dynamics). Thus, the system would exhibit a quantum or classical phase transition in the extreme cases. A previous result

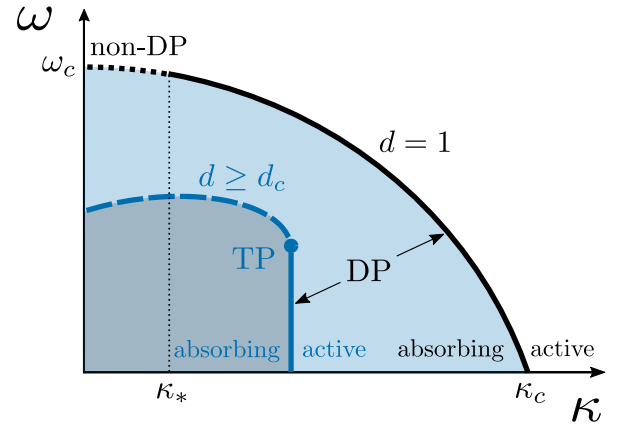


FIG. 1. Schematic phase diagram of the QCP model in the parameter space (κ, ω) in the mean-field limit (inside) and one dimension (outside). For the former, discontinuous (dashed curve) and continuous transitions (solid line) occur, and they meet at a tricritical point (TP). For the latter, a continuous transition occurs over the entire region $[0, \kappa_c]$; however, in the interval $[0, \kappa_*]$, the exponent α of the density of active sites $n(t) \sim t^{-\alpha}$ decreases continuously as κ is increased with non-DP values. In the region $\kappa \in [\kappa_*, \kappa_c]$, it has the DP value.

based on the mean-field solution [34] showed that the QCP exhibits a continuous (discontinuous) phase transition when κ is large (small). Thus, a tricritical point exists, as shown in Fig. 1. This result is similar to the phase diagram generated by the so-called tricritical CP explored in classical systems [41]. We remark that the absorbing phase transition of the classical CP belongs to the directed percolation (DP) universality class.

A recent numerical study of the 1D-QCP with $\kappa = 0$ [38–40] revealed that only a continuous transition occurs. Moreover, when the QCP starts from a homogeneous state, i.e., all the sites are in the active state, the density of active sites at time t , denoted as $n(t)$, decays as $n(t) \sim t^{-\alpha}$ at the transition point ω_c for $\kappa = 0$. The exponent α was estimated as ≈ 0.36 , which differs from the DP value, ≈ 0.16 . Thus, it was argued that the 1D-QCP produces a novel critical behavior. This result was obtained using the tensor network algorithm.

In this Letter, we confirm the above result and further show

that there exists an interval $[0, \kappa_*]$ in which the exponent α decreases continuously as κ is increased, and that for $\kappa \geq \kappa_*$, it has the DP value. The phase diagram for the 1D-QCP is shown in Fig. 1. We obtain this result using the quantum jump Monte Carlo (QJMC) method [49–55]. Moreover, using the neural network (NN) machine learning algorithm, we determine the transition point $\omega_c(\kappa)$ for each κ . Applying finite-size scaling (FSS) analysis, we determine the exponent ν_\perp associated with the correlation length. The value of this exponent also deviates from the previous result [38, 39]; however, it is consistent with the DP value within the error bars. We find that when the 1D-QCP starts from a single active site, all the critical exponents are consistent with the DP values. On the basis of these results, it seems that when the 1D-QCP starts in a homogeneous state, the quantum coherence is long-ranged, and it plays a role similar to that of the Lévy flight long-range interaction in the tricritical CP. When an active site interacts with an inactive site at a distance r with rate $\kappa P(r) \sim \kappa/r^{d+\sigma}$ in one dimension [36, 47, 56], the exponent α depends on σ in an appropriate range of σ . We will discuss this in detail later.

Method – The NN approach has recently served as a powerful tool [57, 58] for classifying the phases in classical systems [59]. In this case, the occupation of each element is represented by a binary value. However, in quantum systems, it is represented by a real value; thus, the collective pattern is more complex. Nevertheless, the supervised NN approach to quantum systems has reportedly been used successfully to identify the transition point of closed quantum systems [60–65]. Here, we use this approach for the first time to identify the transition point $\omega_c(\kappa)$ in a dissipative phase transition. The details of the NN approach we used are presented in the supplementary material (SM) [66].

We first take labeled snapshots of the 1D-QCP generated by QJMC simulations of a finite system far from a transition point in both directions and organize them in datasets; the well-optimized NNs then respond sensitively to the transition point. This supervised learning method correctly identifies the position of the transition point. Second, using the obtained transition points $\omega_c(N)$ for given system sizes, we perform FSS analysis and identify the transition point in the thermodynamic limit ω_c . We also determine the correlation length exponent ν_\perp . Next, we determine the other critical exponents by performing extensive QJMC simulations of a large system at ω_c .

Model – We consider a one-dimensional quantum spin chain with a periodic boundary condition, where each state of a site, either active or inactive, represents the up or down spin state, denoted as $|\uparrow\rangle$ or $|\downarrow\rangle$. The time evolution of the density matrix $\hat{\rho}$ is described by the Lindblad equation, which consists of the Hamiltonian and dissipative terms [67]:

$$\partial_t \hat{\rho} = -i[\hat{H}_S, \hat{\rho}] + \sum_{\ell=1}^N \left[\hat{L}_\ell^{(d)} \hat{\rho} \hat{L}_\ell^{(d)\dagger} - \frac{1}{2} \{ \hat{L}_\ell^{(d)\dagger} \hat{L}_\ell^{(d)}, \hat{\rho} \} \right]. \quad (1)$$

The Hamiltonian \hat{H}_S , which governs the branching and coagulation processes and represents coherent interactions, is expressed as

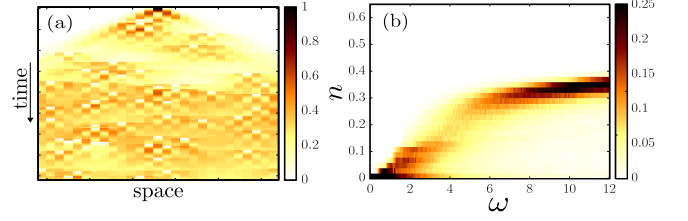


FIG. 2. (a) Trajectory of the 1D-QCP with $\kappa = 0$ and $\omega > \omega_c$ from a single active site at the center. (b) Histogram of the densities of active sites in steady states as a function of ω for system size $N = 20$. The data are obtained using QJMC simulations. Time t and the control parameter ω are given in units of $1/\gamma$ and γ , respectively.

pressed as $\hat{H}_S = \omega \sum_{\ell=1}^N [(\hat{n}_{\ell-1} + \hat{n}_{\ell+1}) \hat{\sigma}_\ell^x]$.

The Lindblad decay, branching, and coagulation operators are given by $\hat{L}_\ell^{(d)} = \sqrt{\gamma} \hat{\sigma}_\ell^-$, $\hat{L}_\ell^{(b)} = \sqrt{\kappa} (\hat{n}_{\ell-1} + \hat{n}_{\ell+1}) \hat{\sigma}_\ell^+$, and $\hat{L}_\ell^{(c)} = \sqrt{\kappa} (\hat{n}_{\ell-1} + \hat{n}_{\ell+1}) \hat{\sigma}_\ell^-$, respectively. $\hat{\sigma}_\ell^+$ and $\hat{\sigma}_\ell^-$ are the raising and lowering operators of the spin at site ℓ , respectively; they are defined in terms of the spin basis as $\hat{\sigma}_\ell^+ = |\uparrow\rangle\langle\downarrow|$ and $\hat{\sigma}_\ell^- = |\downarrow\rangle\langle\uparrow|$. In addition, $\hat{n} = \hat{\sigma}^+ \hat{\sigma}^-$ and $\hat{\sigma}^x = \hat{\sigma}^+ + \hat{\sigma}^-$ are the number operator and spin flip operator, respectively.

Quantum branching and coagulation occur at a rate ω , and the corresponding classical processes occur at a rate κ . When $\omega \rightarrow 0$, the model is reduced to the classical CP, which belongs to the DP class. Here, we first consider the pure quantum limit $\kappa \rightarrow 0$ but with finite ω . The opposite limit $\omega \rightarrow 0$ with finite κ , and the case of both ω and κ being finite are discussed in the SM [66]. In addition, we rescale time and the quantum control parameter ω in units of γ ; therefore, we set $\gamma = 1$.

When ω is small, inactive particles become more abundant with time, and eventually the system is fully occupied by inactive particles. Thus, the system is no longer dynamic and falls into an absorbing state, which is represented by $\hat{\rho}_{\text{ab}} = |\downarrow \cdots \downarrow\rangle\langle\downarrow \cdots \downarrow|$. When ω is large, the system remains in an active state with a finite density of active particles [Fig. 2(a)]. Thus, the QCP exhibits a phase transition from an active to an absorbing state as the control parameter ω is decreased. As shown in Fig. 2(b), the phase transition seems to be continuous. In fact, it was conjectured that the 1D-QCP exhibits a continuous transition [37]. The transition point and spatial correlation length exponent were obtained numerically using the tensor network approach as $\omega_c = 6.0 \pm 0.05$ and $\nu_\perp = 0.5 \pm 0.2$ [38], respectively. By contrast, the values we obtained using the NN approach are $\omega_c \approx 6.04$ and $\nu_\perp = 1.06 \pm 0.04$.

To implement the NN approach, we first organize a dataset of the occupation probability of site ℓ , which is denoted as $p_\ell(t) = \text{Tr}[\hat{\rho}(t) \hat{n}_\ell]$. Using the QJMC method, we generate a steady-state configuration and obtain the occupation probabilities of each site, $\{p_\ell\}$. We collect 5×10^3 configurations in $\omega \in [0, 12]$ at $\Delta\omega = 0.04$ intervals. To prepare the training dataset for supervised learning, we label the configurations using one-hot encoding [68], where the absorb-

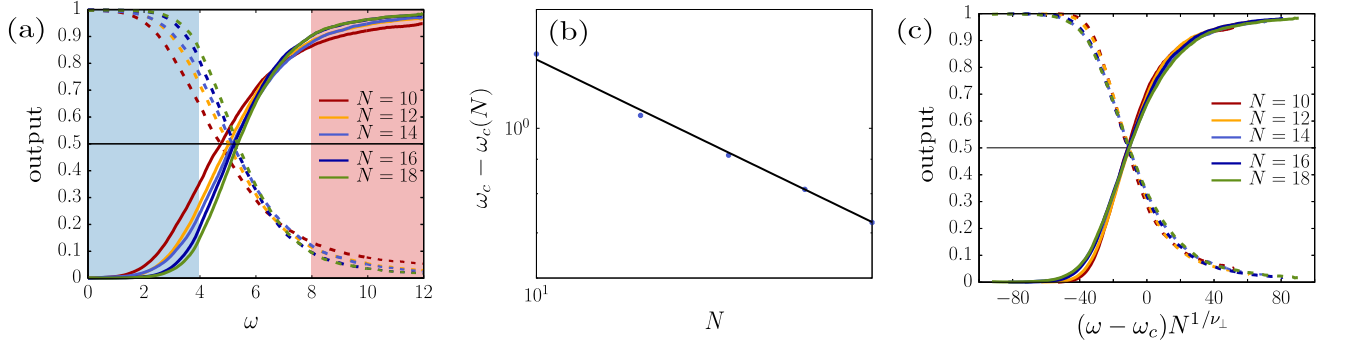


FIG. 3. (a) Plot of the output averaged over a test set as a function of ω for different system sizes. Solid (dashed) line represents the values of the first (second) output neuron. From this plot, we estimate the crossing point of the two outputs and regard it as the transition point $\omega_c(N)$ for a given system size N . (b) Plot of $\omega_c - \omega_c(N)$ versus N , where ω_c is chosen so as to yield power-law behavior and is regarded as the transition point in the thermodynamic limit. The slope represents the value of the critical exponent $-1/\nu_\perp$. (c) Scaling plot of the output versus $(\omega - \omega_c)N^{1/\nu_\perp}$. For the obtained numerical values of ν_\perp and ω_c , the data collapse well for system sizes $N = 10, 12, 14, 16$, and 18 .

ing state ($\omega \in [0, 4]$) is encoded as $(0, 1)$, and the active state ($\omega \in [8, 12]$) is encoded as $(1, 0)$ [see shaded regions in Fig. 3(a)].

Next, to train the machine, we construct the hidden layers of the convolutional NN (CNN), including the one-dimensional convolutional layers [69], batch normalization layers [70], and fully connected layers. When the NN is well-trained with the labeled training dataset in the two regions, we obtain the outputs for the entire ω region. More details are presented in the SM [66].

Finite-size scaling – In Fig. 3(a), the two outputs indicate the predictabilities that the system will fall into the absorbing state and remain in the active state, respectively. The crossing point of these outputs indicates a transition point $\omega_c(N)$ for a given system size N [Fig. 3(a)]. Using the obtained $\omega_c(N)$ for different system sizes, we determine ω_c in the thermodynamic limit by plotting $\omega_c - \omega_c(N)$ versus N [Fig. 3(b)], which is expected to behave as $\omega_c - \omega_c(N) \sim N^{-1/\nu_\perp}$. Indeed, the plot exhibits power-law behavior when an appropriate value of ω_c is chosen, and the critical exponent ν_\perp is obtained from the slope of the power-law curve. We obtain $\omega_c \approx 6.04$ and $\nu_\perp = 1.06 \pm 0.04$; the latter is in agreement with the value of $\nu_\perp \approx 1.096$ for the DP class in one dimension, but differs from the value of $\nu_\perp \approx 0.5 \pm 0.2$ obtained using the tensor network approach. Finally, the scaling plot is drawn in the form of the output versus $(\omega - \omega_c)N^{1/\nu_\perp}$ for different N values [Fig. 3(c)]. The data for different system sizes seem to collapse.

Next, we measure the values of the other critical exponents using the numerical data obtained by the QJMC method in the critical region around ω_c . First, we take an initial state in which a single active seed is present at $\ell = 0$, and the remaining sites are inactive. This configuration is expressed as $\hat{\rho}(0) = \hat{\sigma}_0^+ \rho_{ab} \hat{\sigma}_0^-$. We measure the following quantities: i) the survival probability, that is, the probability that the system does not fall into an absorbing state, $P(t) = 1 - \text{Tr}[\hat{\rho}(t)\hat{\rho}_{ab}]$; ii) the number of active sites, $N_a(t) = \sum_\ell \text{Tr}[\hat{\rho}(t)\hat{n}_\ell]$; iii) the mean square distance of the active sites from the origin, $R^2(t) = \sum_\ell \text{Tr}[\ell^2 \hat{\rho}(t)\hat{n}_\ell]/N_a(t)$; iv) the density of seed-site over

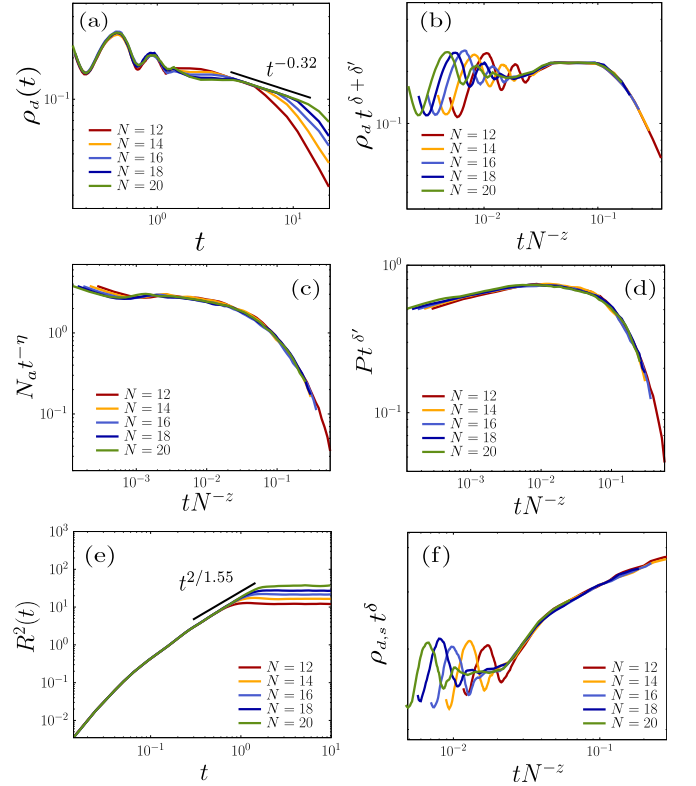


FIG. 4. Estimates of the critical exponents of the 1D-QCP starting from a single active site. (a) Plot of $\rho_d(t)$ versus t , which behaves as $\rho_d(t) \sim t^{-\delta-\delta'}$. (b) Scaling plot of $\rho_d(t)t^{\delta+\delta'}$ versus tN^{-z} for $\delta + \delta' = 0.32$ and $z = 1.55$. (c) Scaling plot of $N_a(t)t^{-\eta}$ versus tN^{-z} for $\eta = 0.30$ and $z = 1.55$. (d) Scaling plot of $P(t)t^{\delta'}$ versus tN^{-z} for $\delta' = 0.16$ and $z = 1.55$. (e) Plot of $R^2(t)$ as a function of t . (f) Scaling plot of $\rho_{d,s}(t)t^\delta$ versus tN^{-z} for $\delta = 0.16$ and $z = 1.55$.

all runs, $\rho_d(t) = \text{Tr}[\hat{\rho}(t)\hat{n}_{\ell=0}] \sim N_a(t)/R(t)$; and v) the density of seed-site over surviving runs, $\rho_{d,s}(t) = \rho_d(t)/P(t)$. At the transition point, these quantities exhibit the following power-law behaviors: $P(t) \propto t^{-\delta'}$, $N_a(t) \propto t^\eta$, $R^2(t) \propto t^{2/z}$, $\rho_d(t) \propto t^{\eta-1/z}$,

and $\rho_{d,s}(t) \propto t^{-\delta}$. For the relation $\rho_d(t) = \rho_{d,s}(t)P(t) \sim t^{-\delta-\delta'}$, the scaling relation $\eta - 1/z = -(\delta + \delta')$ holds [71]. We estimate the exponents $\delta + \delta'$, η , δ' , z , and δ by direct measurement of the slopes in the double-logarithmic plots, as shown in Fig. 4. We estimate the exponent z using the data collapse technique. For instance, for the survival probability $P(t)$, we plot $P(t)t^{\delta'}$ versus tN^{-z} for different system sizes N . We determine z as the value at which the data for different system sizes collapse onto a single curve. The values of critical exponents are in good agreement with the DP values within the error bars (Table I).

Second, we take a homogeneous initial state in which the entire system is occupied by active sites at $t = 0$, which is expressed as $\hat{\rho}(0) = |\uparrow \cdots \uparrow\rangle\langle \uparrow \cdots \uparrow|$. From this initial state, we measure vi) the density $n(t)$ of active sites at time t averaged over all runs. This quantity is formulated as $n(t) = (\sum_{\ell} \text{Tr}[\hat{\rho}(t)\hat{n}_{\ell}])/N$. We find that $n(t)$ exhibits power-law decay as $n(t) \sim t^{-\alpha}$ with the exponent $\alpha = 0.32 \pm 0.01$, as shown in Fig. 5. This value is consistent with the result obtained by applying the tensor network approach; however, it is not consistent with the corresponding DP value, which was estimated as $\alpha_{\text{DP}} = 0.16$. Therefore, the 1D-QCP with $\kappa = 0$ creates a novel universality class.

We note that $\rho_d(t)$ and $n(t)$ are actually the same quantity even though they emerge from different initial states. They exhibit the same critical behaviors in the CP class (see the SM [66]), but they exhibit different critical behaviors for the 1D-QCP. This behavior is unusual, because the universality class is independent of the initial state according to the theory of critical phenomena. To understand the underlying mechanism, we increase the control parameter κ from zero to $\kappa = 0.6$ in steps of 0.2 and explore the behavior of $n(t)$ at each $\omega_c(\kappa)$. We find that the value of α decreases continuously from 0.32 for $\kappa = 0$ to $\alpha = 0.16$ for $\kappa = 0.6$. The details are presented in the SM [66]. These results suggest that α varies continuously as κ is increased and reaches the DP value at $\kappa_* \approx 0.58$. When $\kappa = 0$ and all the sites are active at $t = 0$, the wave functions of each site overlap, and thus the entire system becomes coherent. This quantum effect is extremely strong when $\kappa = 0$. As κ is increased, this long-range coherence is gradually reduced. This finding may be related to the behavior that occurs in the tricritical CP with power-law interactions: Each active particle activates an inactive particle at distance r with rate $\kappa/r^{d+\sigma}$, where d is the spatial dimension, and σ is a parameter. Then, the critical exponent α depends on the power σ in an appropriate range of σ . As σ is increased, the effect of long-range interactions becomes weaker, and the exponent α becomes smaller [56].

Summary and Discussion – We investigated the phase transitions arising in the 1D-QCP as a prototypical example of dissipative phase transitions. The phase diagram was obtained (Fig. 1) in the parameter space spanned by κ and ω , which represent the contributions of the classical and quantum effects, respectively. The curve of the transition between the absorbing and active phases has two parts: the non-DP region $[0, \kappa_*]$ and the DP region $[\kappa_*, \kappa_c]$. In the non-DP region,

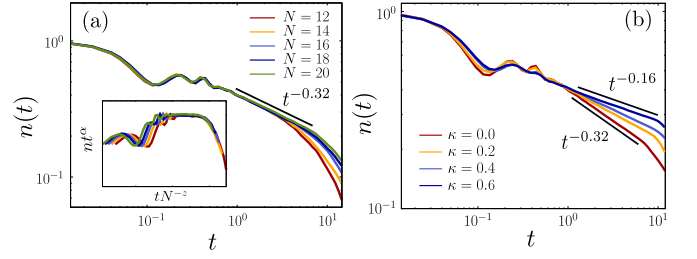


FIG. 5. Estimates of the critical exponent α from the homogeneous state. (a) Plot of $n(t)$ as a function of t for different system sizes, which shows that $n(t) \sim t^{-\alpha}$. The inset shows the scaling plot of $n(t)t^{\alpha}$ versus tN^{-z} for $\alpha = 0.32$ and $z = 1.55$. (b) Plot of $n(t)$ as a function of t for different κ in the range $\kappa \in [0, 0.6]$ in steps of 0.2.

TABLE I. Critical point and critical exponents for the 1D-QCP.

	1D-QCP from CNN+QJMC	1D-QCP from tensor network [38, 39]	1D-DP
ω_c	6.04	6.0 ± 0.05	—
δ'	0.16 ± 0.05	0.26 ± 0.04	0.159
z	1.55 ± 0.06	1.61 ± 0.16	1.581
η	0.30 ± 0.05	0.26 ± 0.05	0.313
$\delta + \delta'$	0.32 ± 0.01	0.36 ± 0.12	0.318
α	0.32 ± 0.01	0.36 ± 0.08	0.159
ν_{\perp}	1.06 ± 0.04	0.5 ± 0.2	1.096

the critical exponent α , which is associated with the density of active sites $n(t)$ for a homogeneous initial state, decreases continuously as κ is increased. It is also interesting that the discontinuous transition near $\kappa = 0$ in the mean-field limit changes to a continuous transition with a continuously varying exponent in one dimension.

Acknowledgements – This research was supported by the NRF, Grant No. NRF-2014R1A3A2069005 and the AI Institute of Seoul National University (AIIS) through its AI Frontier Research Grant in 2020 (BK). MJ would like to thank E. Gillman for helpful discussions.

* bkahnng@snu.ac.kr

- [1] I. Carusotto and C. Ciuti, Rev. Mod. Phys. **85**, 299 (2013).
- [2] C. Noh and D. G. Angelakis, Rep. Prog. Phys. **80**, 016401 (2017).
- [3] H. J. Carmichael, Phys. Rev. X **5**, 031028 (2015).
- [4] M. Fitzpatrick, N. M. Sundaresan, A. C. Y. Li, J. Koch, and A. Houck, Phys. Rev. X **7**, 011016 (2017).
- [5] C. Pérez-Espigares, M. Marcuzzi, R. Gutiérrez, and I. Lesanovsky, Phys. Rev. Lett. **119**, 140401 (2017).
- [6] S. Helmrich, A. Arias, G. Lochead, T. M. Wintermantel, M. Buchhold, S. Diehl, and S. Whitlock, Nature **577**, 481 (2020).
- [7] T. E. Lee, S. Gopalakrishnan, and M. D. Lukin, Phys. Rev. Lett. **110**, 257204 (2013).
- [8] J. Jin, A. Biella, O. Viyuela, L. Mazza, J. Keeling, R. Fazio, and D. Rossini, Phys. Rev. X **6**, 031011 (2016).
- [9] A. Le Boité, G. Orso, and C. Ciuti, Phys. Rev. Lett. **110**, 233601 (2013).

- [10] J. Klinder, H. Keßler, M. Wolke, L. Mathey, and A. Hemmerich, *Proc. Natl. Acad. Sci. U. S. A.* **112**, 3290 (2015).
- [11] L. J. Zou, D. Marcos, S. Diehl, S. Putz, J. Schmiedmayer, J. Majer, and P. Rabl, *Phys. Rev. Lett.* **113**, 023603 (2014).
- [12] D. Nagy and P. Domokos, *Phys. Rev. Lett.* **115**, 043601 (2015).
- [13] A. A. Houck, H. E. Tureci, and J. Koch, *Nat. Phys.* **8**, 292 (2012).
- [14] M. Müller, S. Diehl, G. Pupillo, and P. Zoller, *Adv. At. Mol. Opt. Phys.* **61**, 1 (2012).
- [15] K. Baumann, C. Guerlin, F. Brennecke, and T. Esslinger, *Nature* **464**, 1301 (2010).
- [16] K. Baumann, R. Mottl, F. Brennecke, and T. Esslinger, *Phys. Rev. Lett.* **107**, 140402 (2011).
- [17] I. Bloch, *Nat. Phys.* **1**, 23 (2005).
- [18] J. M. Fink, A. Dombi, A. Vukics, A. Wallraff, and P. Domokos, *Phys. Rev. X* **7**, 011012 (2017).
- [19] T. Fink, A. Schade, S. Höfling, C. Schneider, and A. Imamoglu, *Nat. Phys.* **14**, 365 (2018).
- [20] E. G. Dalla Torre, E. Demler, T. Giamarchi, and E. Altman, *Nat. Phys.* **6**, 806 (2010).
- [21] L. M. Sieberer, S. D. Huber, E. Altman, and S. Diehl, *Phys. Rev. Lett.* **110**, 195301 (2013).
- [22] L. M. Sieberer, S. D. Huber, E. Altman, and S. Diehl, *Phys. Rev. B* **89**, 134310 (2014).
- [23] S. Diehl, A. Tomadin, A. Micheli, R. Fazio, and P. Zoller, *Phys. Rev. Lett.* **105**, 015702 (2010).
- [24] U. C. Täuber and S. Diehl, *Phys. Rev. X* **4**, 021010 (2014).
- [25] J. Marino and S. Diehl, *Phys. Rev. Lett.* **116**, 070407 (2016).
- [26] J. Lang and F. Piazza, *Phys. Rev. A* **94**, 033628 (2016).
- [27] R. Rota, F. Minganti, C. Ciuti, and V. Savona, *Phys. Rev. Lett.* **122**, 110405 (2019).
- [28] E. G. D. Torre, S. Diehl, M. D. Lukin, S. Sachdev, and P. Strack, *Phys. Rev. A* **87**, 023831 (2013).
- [29] W. Verstraelen, R. Rota, V. Savona, and M. Wouters, *Phys. Rev. Res.* **2**, 022037(R) (2020).
- [30] A. Mitra, S. Takei, Y. B. Kim, and A. J. Millis, *Phys. Rev. Lett.* **97**, 236808 (2006).
- [31] E. G. Dalla Torre, E. Demler, T. Giamarchi, and E. Altman, *Phys. Rev. B* **85**, 184302 (2012).
- [32] R. Rota, F. Storme, N. Bartolo, R. Fazio, and C. Ciuti, *Phys. Rev. B* **95**, 134431 (2017).
- [33] We would like to thank an anonymous referee for providing this overall view.
- [34] M. Marcuzzi, M. Buchhold, S. Diehl, and I. Lesanovsky, *Phys. Rev. Lett.* **116**, 245701 (2016).
- [35] M. Buchhold, B. Everest, M. Marcuzzi, I. Lesanovsky, and S. Diehl, *Phys. Rev. B* **95**, 014308 (2017).
- [36] M. Jo, J. Um, and B. Kahng, *Phys. Rev. E* **99**, 032131 (2019).
- [37] D. Roscher, S. Diehl, and M. Buchhold, *Phys. Rev. A* **98**, 062117 (2018).
- [38] F. Carollo, E. Gillman, H. Weimer, and I. Lesanovsky, *Phys. Rev. Lett.* **123**, 100604 (2019).
- [39] E. Gillman, F. Carollo, and I. Lesanovsky, *New J. Phys.* **21**, 093064 (2019).
- [40] E. Gillman, F. Carollo, and I. Lesanovsky, *arXiv:2002.09238 [quant-ph]* (2020).
- [41] R. Dickman and I. Jensen, *Phys. Rev. Lett.* **67**, 2391 (1991).
- [42] R. M. Ziff, E. Gulari, and Y. Barshad, *Phys. Rev. Lett.* **56**, 2553 (1986).
- [43] J. Marro and R. Dickman, *Nonequilibrium Phase Transitions in Lattice Models*, (Cambridge University Press, Cambridge 2005).
- [44] T. E. Harris, *Ann. Probab.* **2**, 969 (1974).
- [45] G. Ódor, *Rev. Mod. Phys.* **76**, 663 (2004).
- [46] M. Henkel, H. Hinrichsen, and S. Lübeck, *Non-Equilibrium Phase Transitions*, Theoretical and Mathematical Physics, Vol. 1 (Springer, Netherlands 2009).
- [47] H. Hinrichsen, *Adv. Phys.* **49**, 815 (2000).
- [48] R. Gutiérrez, C. Simonelli, M. Archimi, F. Castellucci, E. Arimondo, D. Ciampini, M. Marcuzzi, I. Lesanovsky, and O. Morsch, *Phys. Rev. A* **96**, 041602(R) (2017).
- [49] R. Dum, P. Zoller, and H. Ritsch, *Phys. Rev. A* **45**, 4879 (1992).
- [50] N. Gisin and I. C. Percival, *J. Phys. A* **25**, 5677 (1992).
- [51] J. Dalibard, Y. Castin, and K. Mølmer, *Phys. Rev. Lett.* **68**, 580 (1992).
- [52] K. Mølmer, Y. Castin, and J. Dalibard, *J. Opt. Soc. Am. B* **10**, 524 (1993).
- [53] H.-P. Breuer and F. Petruccione, *Phys. Rev. A* **55**, 3101 (1997).
- [54] M. B. Plenio and P. L. Knight, *Rev. Mod. Phys.* **70**, 101 (1998).
- [55] A. J. Daley, *Adv. Phys.* **64**, 77 (2014).
- [56] M. Jo and B. Kahng, *Phys. Rev. E* **101**, 022121 (2020).
- [57] Y. LeCun, Y. Bengio, and G. Hinton, *Nature* **521**, 436 (2015).
- [58] G. Carleo, I. Cirac, K. Cranmer, L. Daudet, M. Schuld, N. Tishby, L. Vogt-Maranto, and L. Zdeborová, *Rev. Mod. Phys.* **91**, 045002 (2019).
- [59] J. Carrasquilla and R. G. Melko, *Nat. Phys.* **13**, 431 (2017).
- [60] P. Broecker, J. Carrasquilla, R. G. Melko, and S. Trebst, *Sci. Rep.* **7**, 8823 (2017).
- [61] K. Ch'ng, J. Carrasquilla, R. G. Melko, and E. Khatami, *Phys. Rev. X* **7**, 031038 (2017).
- [62] J. Venderley, V. Khemani, and E.-A. Kim, *Phys. Rev. Lett.* **120**, 257204 (2018).
- [63] A. Canabarro, F. F. Fanchini, A. L. Malvezzi, R. Pereira, and R. Chaves, *Phys. Rev. B* **100**, 045129 (2019).
- [64] B. S. Rem, N. Käming, M. Tarnowski, L. Asteria, N. Fläschner, C. Becker, K. Sengstock, and C. Weitenberg, *Nat. Phys.* **15**, 917 (2019).
- [65] A. Bohrdt, C. S. Chiu, G. Ji, M. Xu, D. Greif, M. Greiner, E. Demler, F. Grusdt, and M. Knap, *Nat. Phys.* **15**, 921 (2019).
- [66] See Supplemental Material for more details. First, the structure of our NN and the optimization scheme are presented. Second, the continuously varying exponent α is discussed more thoroughly. Third, we describe the FSS of the classical CP using the QJMC method. Fourth, the relation $\delta = \alpha$ for the classical CP and classical tricritical CP is presented with other critical exponents. Next, we estimate the critical exponent associated with the temporal correlation $\nu_{||}$, which is helpful for confirming the critical exponent $\nu_{\perp} = \nu_{||}/z$. Finally, the results of the NN approach for different training regions are presented.
- [67] H.-P. Breuer and F. Petruccione, *The Theory of Open Quantum Systems*, (Oxford University Press, Oxford 2007).
- [68] D. Harris and S. Harris, *Digital Design and Computer Architecture*, 2nd ed. (Morgan Kaufmann Publishers Inc., San Francisco 2012).
- [69] S. Kiranyaz, T. Ince, R. Hamila, and M. Gabbouj, 37th Annual International Conference of the IEEE Engineering in Medicine and Biology Society (EMBC), Milan, 2015 (2015).
- [70] S. Ioffe and C. Szegedy, *arXiv:1502.03167v3 [cs.LG]* (2015).
- [71] J. F. F. Mendes, R. Dickman, M. Henkel, and M. C. Marques, *J. Phys. A* **27**, 3019 (1994).

Supplementary Material to Absorbing phase transition with a continuously varying exponent in quantum contact process

NEURAL NETWORK APPROACH

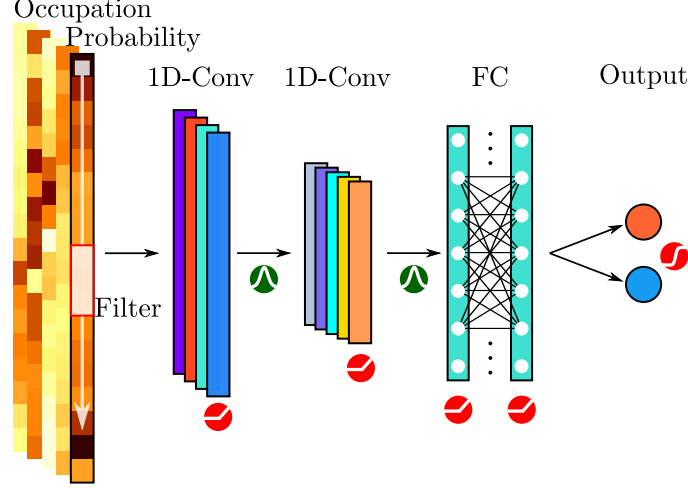


FIG. S1. Schematic illustration of the convolutional neural network built in combination of a one-dimensional convolutional layer (1D-Conv) and a fully connected layer (FC). The red circles represent the activation function of each layer. The green circles below the arrows represent the batch normalization.

In the main text, we mentioned that the supervised NN approach has not been applied in dissipative phase transitions. On the other hand, the unsupervised NN approach has recently been applied to generate the configurations of open quantum systems in steady state using the restricted Boltzmann machine [S1–S5]. However, it is challenging to investigate the critical behaviors using unsupervised learning techniques such as the restricted Boltzmann machine. Thus, we used the supervised NN approach including the convolutional neural network to investigate the critical phenomena of dissipative phase transition.

For classical systems, the transition point of a continuous absorbing transition is normally indicated by the presence of power-law behavior of the order parameter with respect to time [S6, S7]. Consequently, a large system size is required to identify the transition point. Accurately identifying the transition point using QJMC simulations of the QCP is even more difficult and is thus a challenging problem. To overcome this difficulty, we notice that the system is in the absorbing state for $\omega \ll \omega_c$ and in the active state for $\omega \gg \omega_c$. Combining this observation with a recently proposed NN supervised learning concept, we identify the transition point. The details of our neural network is as follows.

The objective of the learning procedure is to optimize the neural network to adjust the weights of connections between neural units to achieve a variational minimization of a properly defined cost function. To this end, we collected the snapshots presented in the main text and we construct the hidden layers of the NN, including one-dimensional convolutional layers, batch normalization layers, and fully connected layers, as shown in Fig. S1. We employ the framework of TENSORFLOW [S8] and use ReLU and tanh for the activation function in the hidden layer. Two neurons in the output layer are used, and a softmax function is used as the activation function in the output layer. We employ the cross-entropy or the mean-square error function as the cost (error) function of the NN, which is then optimized using Adam [S9] or RMSProp [S10]. We change the architecture and optimization algorithms in various ways. Regardless of these changes, the well-trained machines produce consistent results.

CONTINUOUSLY VARYING EXPONENT α

For $\kappa < \kappa_*$, there exists the continuously varying critical exponent α , which is different from the DP class. In this section, we shall perform the finite-size scaling for $\kappa \in [0, 0.58]$ in steps of 0.1 to confirm the continuously varying critical exponent α . At the transition point, we estimate the exponents α by measuring the slopes directly in the double-logarithmic plots as shown in Fig. S2(a). The exponent α continuously increases from 0.16 to 0.32 as κ decreases. Moreover, we confirm those exponents using the data-collapse technique. In Fig. S2(b-g), we plot $n(t)t^\alpha$ versus tN^{-z} for different system sizes N for $\kappa \in [0, 0.58]$ and

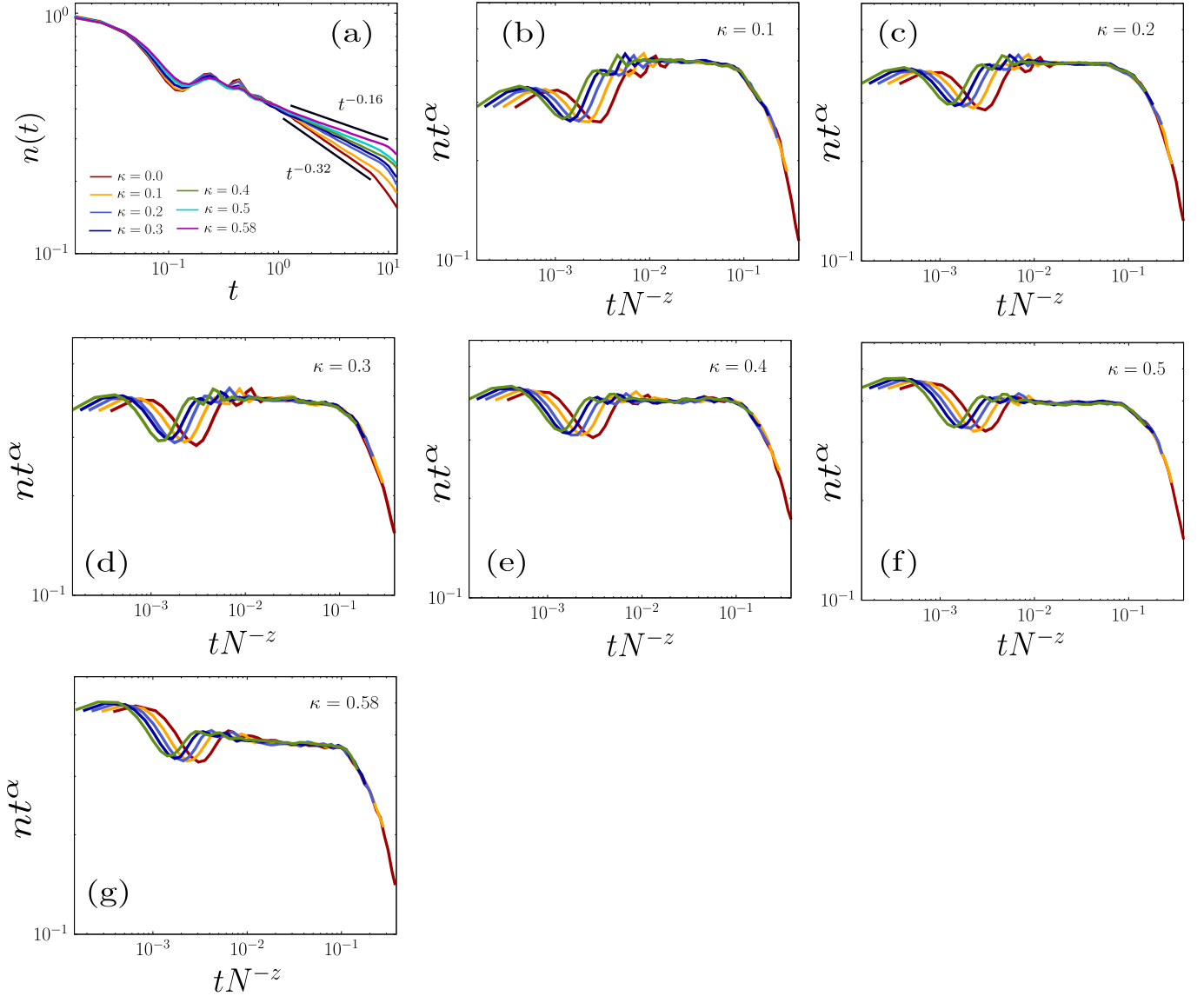


FIG. S2. Estimates of the critical exponents of the 1D-CCP starting from the single active initial state. (a) Plot of $n(t)$ as a function of t for different κ in the range $\kappa \in [0, 0.58]$ in steps of 0.1. The lower (upper) solid line is a guideline with slope -0.32 (-0.16). Scaling plot of $n(t)t^\alpha$ versus tN^{-z} . Incoherent control parameter are taken as $\kappa = 0.1$ for (b), $\kappa = 0.2$ for (c), $\kappa = 0.3$ for (d), $\kappa = 0.4$ for (e), $\kappa = 0.5$ for (f), and $\kappa = 0.58$ for (g). The parameter t is given in units of $1/\gamma$.

TABLE I. Critical exponent α for the 1D-QCP for finite value of κ .

κ	α	δ'	z	η	δ
0.0	0.32 ± 0.01				
0.1	0.28 ± 0.01				
0.2	0.24 ± 0.01				
0.3	0.22 ± 0.01				
0.4	0.20 ± 0.01				
0.5	0.18 ± 0.01				
≥ 0.58		DP values			

the critical exponents are listed in Table I. We remark that the critical exponents except α correspond to the DP values within the

error-bar for this κ region.

CLASSICAL CONTACT PROCESS USING THE QUANTUM JUMP MONTE CARLO METHOD

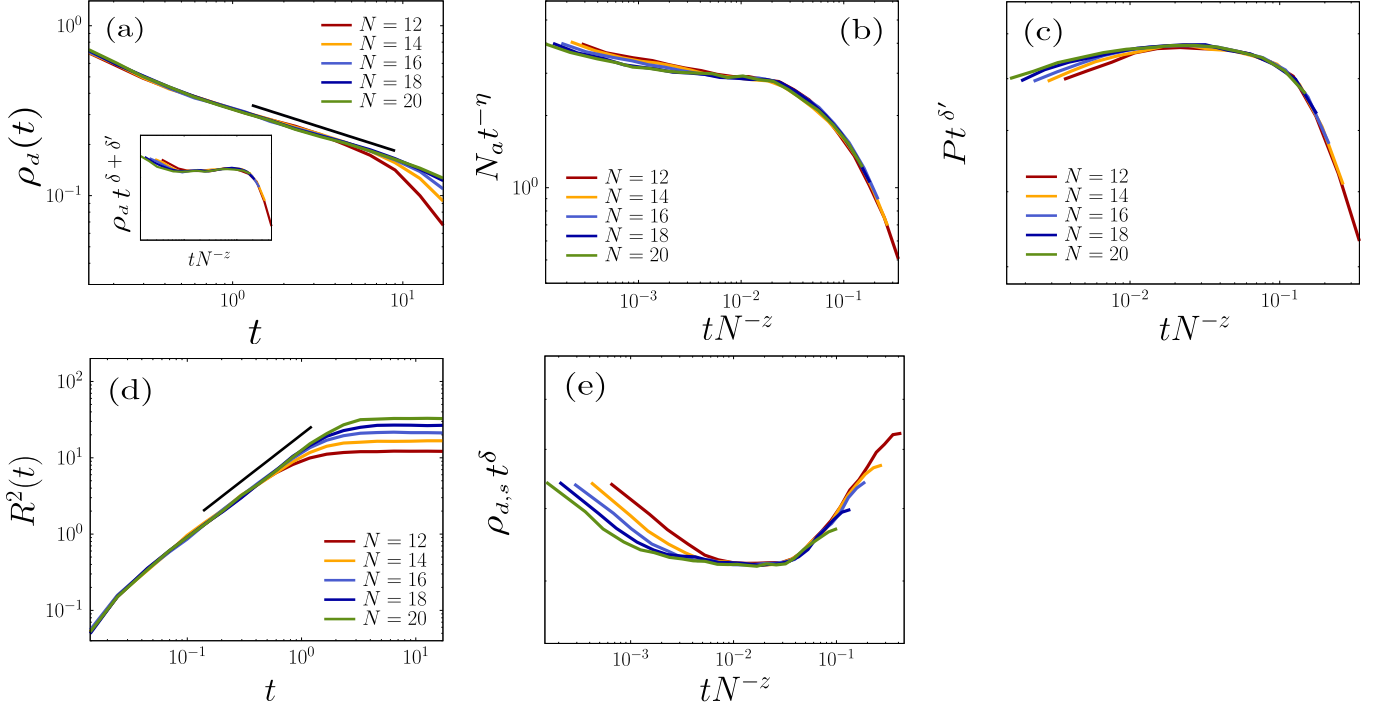


FIG. S3. Estimates of the critical exponents of the 1D-CCP starting from the single active initial state. (a) Plot of $\rho_d(t)$ versus t , which behaves as $\rho_d(t) \sim t^{-\delta-\delta'}$. The solid line is a guideline with slope -0.32 . Inset: scaling plot of $\rho_d(t)t^{\delta+\delta'}$ versus tN^{-z} for $\delta + \delta' = 0.32$ and $z = 1.58$. (b) Scaling plot of $N_a(t)t^{-\eta}$ versus tN^{-z} for $\eta = 0.30$ and $z = 1.58$. (c) Scaling plot of $P(t)t^{\delta'}$ versus tN^{-z} for $\delta' = 0.16$ and $z = 1.58$. (d) Plot of $R^2(t)$ as a function of t . The solid line is a guideline with slope $2/z$ for $z = 1.58$. (e) Scaling plot of $\rho_{d,s}(t)t^{\delta}$ versus tN^{-z} for $\delta = 0.16$ and $z = 1.58$. The parameter t is given in units of $1/\gamma$.

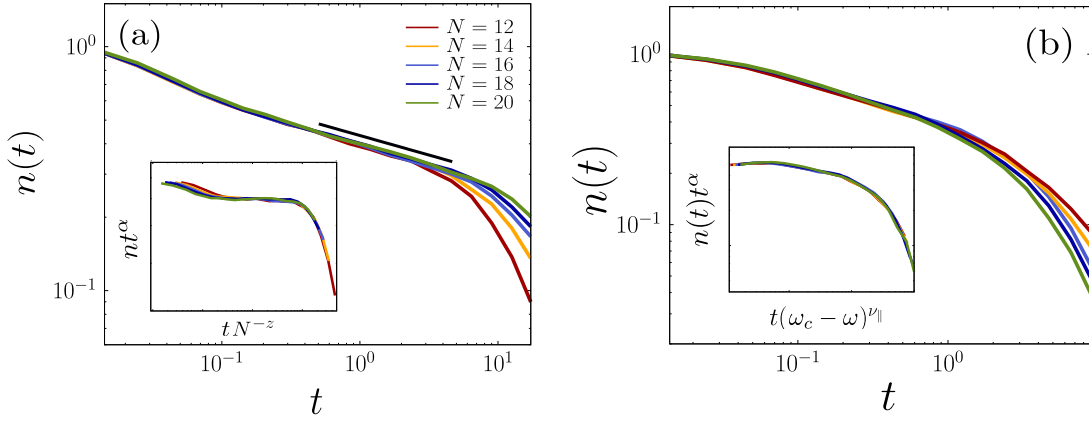


FIG. S4. Estimates of the critical exponents of the 1D-CCP starting from the fully active initial state. (a) Plot of $n(t)$ as a function of t , which shows $n(t) \sim t^{-\alpha}$. The solid line is a guideline with slope -0.16 . Inset: the scaling plot of $n(t)t^{\alpha}$ versus tN^{-z} for $\alpha = 0.16$ and $z = 1.58$. (b) Plot of $n(t)$ as a function of t for different values of $\omega < \omega_c$. Inset: Data points collapse well onto a single curve for $\alpha = 0.16$, and $\nu_{||} = 1.73$. The parameter t is given in units of $1/\gamma$.

The critical exponents of 1D-QCP were obtained using the finite-size scaling from the data of QJMC method in the main text. To check the validity of the finite-size scaling with the small system size, we consider the 1D classical contact process (CCP)

where κ is finite and $\omega = 0$ (see Eqs. (2-5) in the main text). At the critical point, we perform the finite-size scaling to 1D-CCP using the QJMC method. The observables correspond to the definitions of the main text.

First, we obtain the exponents $\delta + \delta'$, η , δ' , z , δ , and α directly by measuring the slopes in the double-logarithmic plots shown in Figs. S3 and S4. Then, we collapse the data by using the obtained exponents to compute the dynamic exponent z . Specifically, we plot $\rho_d t^{\delta+\delta'}$ versus tN^{-z} in Fig. S3(a), $N_a t^{-\eta}$ versus tN^{-z} in Fig. S3(b), and $P(t)t^{-\delta'}$ versus tN^{-z} in Fig. S3(c) for different system sizes N . We measure the exponent z directly using the plot of $R^2(t)$ versus t in Fig. S3(d). In classical contact process, we can classify the surviving runs and thus we measure the exponent $-\delta$ directly using the plot of $\rho_{d,s}(t)$ versus t in Fig. S3(e). Next, we plot $n(t)t^{-\alpha}$ versus tN^{-z} in Fig. S4(a) for different system sizes N . The exponent $\nu_{||}$ is obtained from the rescaling plot of $n(t)t^\alpha$ versus $t(\omega_c - \omega)^{\nu_{||}}$ for different ω values in Fig. S4(b).

The critical exponents are thus obtained as $\delta + \delta' = 0.32 \pm 0.01$, $\eta = 0.31 \pm 0.02$, $\delta' = 0.16 \pm 0.01$, $\delta = 0.16 \pm 0.02$, $z = 1.58 \pm 0.03$, and $\alpha = 0.16 \pm 0.01$. Note that $\delta = \alpha$. In addition, $\alpha = \delta'$ implying that rapidity-reversal symmetry holds. All the critical exponents are in good agreement with the DP values within the error bars. Thus we verified that the critical exponents on classical contact process can be successfully obtained using QJMC method with the same system size in main text.

CRITICAL EXPONENTS IN CLASSICAL ABSORBING PHASE TRANSITION

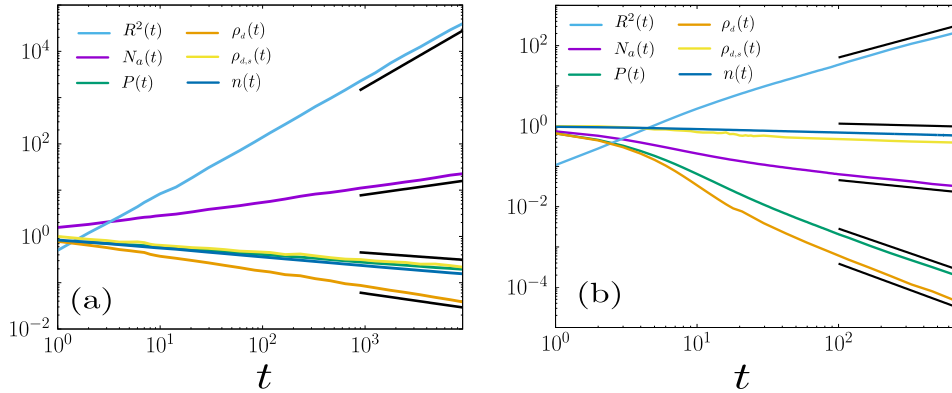


FIG. S5. The behaviors of physical quantities as a function of time t at the transition point. (a) For the classical CP. The solid lines are a guideline with slope $2/z$, η , $-\delta = -\delta' = -\alpha$, $\eta - 1/z$, from top to bottom. The values of all critical exponents are $z = 1.58$, $\delta = 0.16$, $\eta = 0.31$, $\delta' = 0.16$, and $\alpha = 0.16$. Note that $\delta' = \alpha$ and rapidity-reversal symmetry holds. (b) For the 2D classical tricritical contact process starting from a single active site. The solid lines are a guideline with slope $2/z$, $-\delta = -\alpha$, η , $-\delta'$, and $\eta - 1/z$ from top to bottom. The values of all critical exponents are $z = 2.11$, $\delta = 0.09$, $\eta = -0.35$, and $\delta' = 1.21$. Note that rapidity-reversal symmetry is broken.

We mentioned that $\rho_d(t)$ and $n(t)$ show the same asymptotic behavior, which means that $\delta = \alpha$ holds. In this section, we shall check this relation for 1D contact process and 2D tricritical contact process using the classical Monte Carlo simulation. We measure the complete set of critical exponents for the system where rapidity reversal symmetry holds [Fig. S5(a) for 1D contact process] or not [Fig. S5(b) for 2D tricritical contact process]. All critical exponents are successfully obtained and both systems satisfy the relation $\delta = \alpha$. In addition, the generalized hyperscaling relation $\eta - D/z = -\delta - \delta'$, which is believed to be satisfied with the single absorbing state phase transition, holds.

ESTIMATION ON THE CRITICAL EXPONENT $\nu_{||}$ FOR QUANTUM CONTACT PROCESS

We obtained the critical exponent associated with the spatial correlation length $\nu_{\perp} = 1.06 \pm 0.04$ directly from the NN approach. In this section, we verify the critical exponent associated with the spatial correlation ν_{\perp} by obtaining the critical exponent associated with the temporal correlation $\nu_{||} = \nu_{\perp} z$ using QJMC.

The exponent $\nu_{||}$ is obtained from the rescaling plot of $n(t)t^\alpha$ versus $t(\omega_c - \omega)^{\nu_{||}}$ for different ω values. The values of ω are taken from the region used in classical contact process [Fig. S4(b)]. In Fig. S6, we obtain $\nu_{||} = 1.73$ and thus $\nu_{\perp} = \nu_{||}/z \approx 1.095$. This value is consistent with the value from the NN approach.

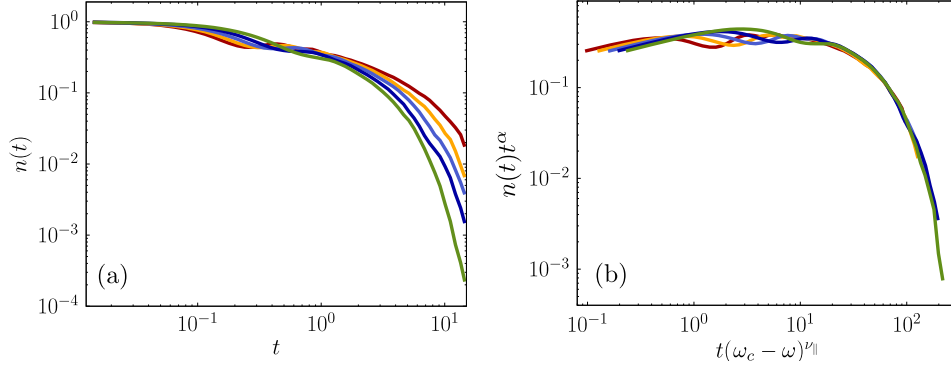


FIG. S6. (a) Plot of $n(t)$ as a function of t for different values of $\omega < \omega_c$. (b) Data points collapse well onto a single curve for $\omega_c = 6.04$, $\alpha = 0.32$, and $\nu_{\parallel} = 1.73$. The units of control parameter is given as γ .

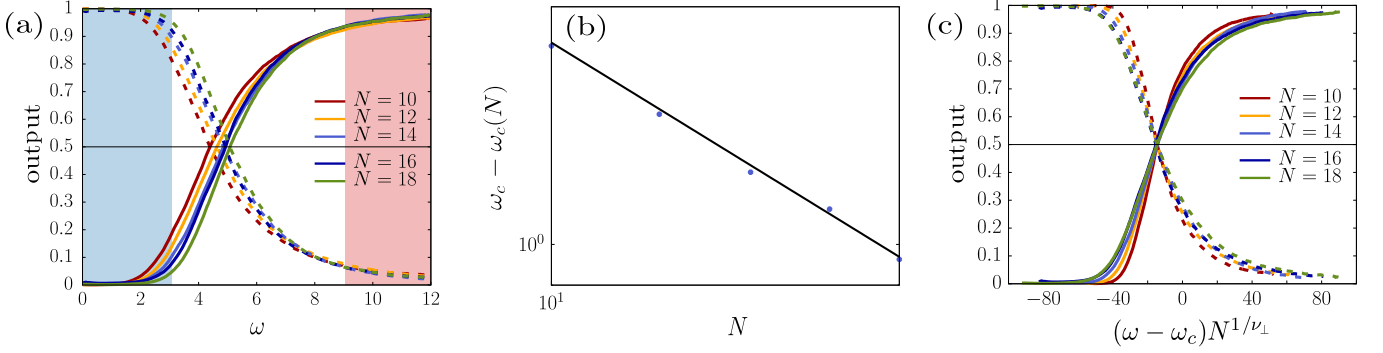


FIG. S7. (a) Plot of the output averaged over a test set as a function of ω for different system sizes. The value of the first (second) output neuron is represented as solid (dashed) line. From this plot, we estimate the crossing point of the two outputs and regard it as the transition point $\omega_c(N)$ for a given system size N . The shaded regions $\omega \in [0, 3]$ and $\omega \in [9, 12]$ indicate the training sets used in the convolutional NN (CNN) analysis. (b) Plot of $\omega_c - \omega_c(N)$ versus N , where ω_c is chosen so as to yield power-law behavior, which is typical near the transition point ω_c . The slope represents the value of the critical exponent $-1/\nu_{\perp}$. (c) Scaling plot of the output versus $(\omega - \omega_c)N^{1/\nu_{\perp}}$. For the obtained numerical values of ν_{\perp} and ω_c , the data collapse well for system sizes $N = 10, 12, 14, 16$, and 18 . From (b) and (c), we obtain $\omega_c \approx 6.04$ and $\nu_{\perp} = 1.06 \pm 0.04$. The units of control parameter is given as γ .

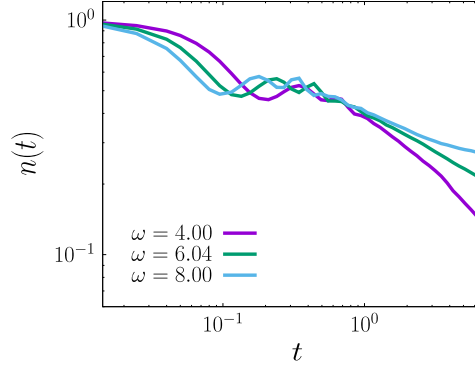


FIG. S8. Plot of $n(t)$ as a function of t for different ω . System size is taken as $N = 20$.

NEURAL NETWORK APPROACH WITH DIFFERENT TRAINING REGION

For supervised learning, it is advantageous to take a narrower test region [white region in Fig. S7(a)], because more information can be taken in the training region. However, if the test region is too narrow to include the crossing point, the crossing point of the outputs would not be the critical point. To avoid this case, it is desirable to take a test region with an appropriate size.

We took the left boundary $\omega = 4$ in the main text, because this is the value at which the order parameter $n(t)$ decays expo-

nentially, i.e., at which the system is in the subcritical region, as shown in Fig. S8. This result was obtained using the QJMC method. However, the boundary $\omega = 8$ was taken, because $n(t)$ behaves as it does in the supercritical state.

To check the sensitivity of the positions of the left and right boundaries, we also considered a test region of ($3 \leq \omega \leq 9$) and then estimated the transition point ω_c in the thermodynamic limit and the value of the exponent ν_{\perp} . As shown in Fig. S7, we obtained the same values of ω_c and ν_{\perp} .

* bkahng@snu.ac.kr

- [S1] M. Schuld, I. Sinayskiy, and F. Petruccione, *Physics* **12**, 74 (2019).
- [S2] M. J. Hartmann and G. Carleo, *Phys. Rev. Lett.* **122**, 250502 (2019).
- [S3] N. Yoshioka and R. Hamazaki, *Phys. Rev. B* **99**, 214306 (2019).
- [S4] A. Nagy and V. Savona, *Phys. Rev. Lett.* **122**, 250501 (2019).
- [S5] F. Vicentini, A. Biella, N. Regnault, and C. Ciuti, *Phys. Rev. Lett.* **122**, 250503 (2019).
- [S6] M. Henkel, H. Hinrichsen, and S. Lübeck, *Non-Equilibrium Phase Transitions*, Theoretical and Mathematical Physics, Vol. 1 (Springer, Netherlands 2009).
- [S7] J. Marro and R. Dickman, *Nonequilibrium Phase Transition in Lattice Models*, (Cambridge University Press, Cambridge 2005).
- [S8] M. Abadi, *et al.* TensorFlow: Large-scale machine learning on heterogeneous systems, arXiv:1603.04467 [cs.DC] (2015).
- [S9] D. P. Kingma and J. Ba, arXiv:1412.6980 (2014).
- [S10] G. Hinton, “Neural Networks for Machine Learning - Lecture 6a - Overview of mini-batch gradient descent.” (2012) <http://www.cs.toronto.edu/~hinton/coursera/lecture6/lec6.pdf>.